AIP Journal of Applied Physics

Roughness analysis in strained silicon-on-insulator wires and films

Ferran Ureña, Sarah H. Olsen, Enrique Escobedo-Cousin, Renato A. Minamisawa, and Jean-Pierre Raskin

Citation: Journal of Applied Physics **116**, 124503 (2014); doi: 10.1063/1.4896301
View online: http://dx.doi.org/10.1063/1.4896301
View Table of Contents: http://scitation.aip.org/content/aip/journal/jap/116/12?ver=pdfcov
Published by the AIP Publishing

Articles you may be interested in
Remote surface roughness scattering in fully depleted silicon-on-insulator devices with high-κ/SiO2 gate stacks
Appl. Phys. Lett. **106**, 023508 (2015); 10.1063/1.4906199

The effect of surface roughness scattering on hole mobility in double gate silicon-on-insulator devices
J. Appl. Phys. **106**, 023705 (2009); 10.1063/1.3176498

Coulomb scattering model for ultrathin silicon-on-insulator inversion layers
Appl. Phys. Lett. **80**, 3835 (2002); 10.1063/1.1477623

Role of surface-roughness scattering in double gate silicon-on-insulator inversion layers
J. Appl. Phys. **89**, 1764 (2001); 10.1063/1.1331076

Surface roughness at the Si–SiO 2 interfaces in fully depleted silicon-on-insulator inversion layers
J. Appl. Phys. **86**, 6854 (1999); 10.1063/1.371763

MIT LINCOLN LABORATORY CAREERS
Discover the satisfaction of innovation and service to the nation
- Space Control
- Air & Missile Defense
- Communications Systems & Cyber Security
- Intelligence, Surveillance and Reconnaissance Systems
- Advanced Electronics
- Tactical Systems
- Homeland Protection
- Air Traffic Control

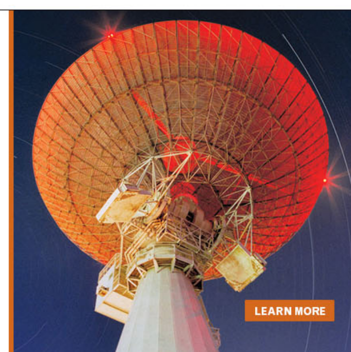

[This article is copyrighted as indicated in the article. Reuse of AIP content is subject to the terms at: http://scitation.aip.org/termsconditions. Downloaded to] IP: 143.106.108.185 On: Mon, 25 May 2015 13:35:19

Roughness analysis in strained silicon-on-insulator wires and films

Ferran Ureña,[1,a)] Sarah H. Olsen,[1] Enrique Escobedo-Cousin,[1] Renato A. Minamisawa,[2] and Jean-Pierre Raskin[3]
[1]*School of Electrical and Electronic Engineering, Newcastle University, Newcastle upon Tyne, United Kingdom*
[2]*Center for Semiconductor Devices, Unicamp, Campinas 13083-870, Brazil*
[3]*Institute of Information and Communication Technologies, Electronics and Applied Mathematics (ICTEAM), Université catholique de Louvain, Louvain-la-Neuve, Belgium*

(Received 18 June 2014; accepted 11 September 2014; published online 22 September 2014)

Strained silicon is used to enhance performance in state-of-the-art CMOS. Under device operating conditions, the effect of strain is to reduce the carrier scattering at the channel by a smoother semiconductor surface. This has never been completely understood. This paper gives first evidence of the variation in surface roughness under realistic strained conditions. At the nanoscale, the SiO_2/Si interface roughness is dependent on the scale of observation (self-affinity). To date, there is no experimental study of the SiO_2/Si interface roughness scaling with strain. This work presents the effect of uniaxial and biaxial strains on the surface roughness of strained silicon-on-insulator films and wires using atomic force microscopy. Levels of strain ranging from 0% to 2.3%, encompassing those used in present CMOS devices have been investigated. It is shown that the silicon surface is affected by uniaxial and biaxial strains differently. Three surface roughness parameters have been analyzed: root mean square roughness, correlation length, and the Hurst exponent, which is used to describe the scaling behavior of a self-affine surface. The results show that the root mean square roughness decreases (up to ∼40%) with increasing tensile strain, whereas the correlation length increases (up to ∼63 nm/%) with increasing tensile strain. The Hurst exponent also varies with strain and with the undulation wavelength regime (between ∼0.8 and 0.2). This dependency explains why some models used to determine the carrier mobility from experiments fit the data better with a Gaussian form, whereas other models fit the data better with an exponential form. © *2014 AIP Publishing LLC*. [http://dx.doi.org/10.1063/1.4896301]

I. INTRODUCTION

In metal-oxide-semiconductor field-effect transistors (MOSFETs), the use of strained silicon channels enhances the mobility of holes and electrons compared with unstrained MOSFET channels.[1,2] Theoretically, the effect of tensile strain is twofold. First, it lowers the symmetry of the crystal by lifting and splitting the degeneracy of the conduction and valence band maxima and minima (thereby reducing intervalley scattering). Second, it reduces the effective mass in the transport direction, which increases carrier mobility.[3] However, while these effects explain the strain-induced mobility enhancement at low vertical electric fields, they do not explain the increase in mobility consistently observed at high vertical electric fields, where devices operate and where surface roughness-limiting mechanisms dominate.[4–6] Modeling work suggests that reduced roughness scattering at high electric field regimes may result from a smoother surface of strained silicon.[7] However, this has never been proven experimentally under reliable conditions and it remains insufficiently understood. This is a major omission since strained silicon has been used in commercial complementary metal-oxide-semiconductor (CMOS) devices since the 90 nm technology node and will be incorporated in future electronic devices including FinFETs and silicon-on-insulator (SOI) and nanowire-based devices.[3]

In order to study the influence of surface roughness scattering limited mobility of electrons and holes under tensile strain, several statistical functions have been used to analyze the surface roughness profile in real space (e.g., height-height correlation function) and in reciprocal space (e.g., power spectral density).[8–10] The experimental data determined from these functions have traditionally been fitted using either a Gaussian or an exponential functional model with two parameters, the root mean square (RMS) surface roughness and the correlation length.[8,11,12] The RMS roughness and the correlation length are used to model the variations of the surface roughness profile in the vertical and horizontal directions, respectively. However, neither the Gaussian nor the exponential model can describe the electron and hole mobility using the same parameters for the RMS roughness and correlation length.[13] In order to describe the mobility of both electrons and holes, alternative expressions have been proposed both in real and reciprocal space.[14,15] These alternative expressions include an additional exponential parameter *n*, which for specific values reduce to the Gaussian and exponential models. No physical meaning has been given to this exponential parameter. Isihara *et al.*[14] studied the silicon interface with pure silicon dioxide (SiO_2) and with oxynitrides ($SiON_x$). They found that different values of the exponential parameter *n* were needed to successfully describe the roughness of both interfaces.[14] To date,

[a)]Author to whom correspondence should be addressed. Electronic mail: ferran.urena@uclouvain.be

[This article is copyrighted as indicated in the article. Reuse of AIP content is subject to the terms at: http://scitation.aip.org/termsconditions. Downloaded to] IP: 143.106.108.185 On: Mon, 25 May 2015 13:35:19

there has been no conclusive study of the relation between the surface roughness exponential parameter n with strain. The relation between the surface roughness exponential parameter n and the different surface models, including the Gaussian and exponential forms, remains poorly understood. It is therefore necessary to develop a complete understanding of the differences in mobility enhancement for electrons and holes with uniaxial and biaxial strains at high electric fields.

The SiO_2/Si interface has been shown to exhibit self-affinity.[16] Self-affinity is an important material characteristic, which has also been omitted from past studies of the strained SiO_2/Si interface. Self-affinity is a property related to fractal objects, which look the same (or statistically the same) after applying a rescaling of the dimensions.[17] In a self-affine surface, the rescaling of the dimensions is connected with the fractal dimension through the Hurst exponent.[18,19] Physically, the Hurst exponent is related to the jaggedness of the surface. In order to completely describe the roughness of a self-affine surface, three parameters are needed: the RMS roughness, the correlation length, and the Hurst exponent.[18,19] For a self-affine surface, Sinha *et al.*[20] proposed a functional form to fit these three parameters extracted from the statistical analysis. The functional form required to fit the experimental data is close to that used in mobility models.[14,15] Despite the strong relation between the functional form used to fit data from a self-affine surface[20] and that used in transport models,[14,15] to date the self-affine behavior of the SiO_2/Si interface has not been considered within mobility studies. Furthermore, there has been no evaluation of the self-affinity of uniaxial and biaxial strained silicon surfaces. Mobility models of both bulk and unstrained silicon devices may be improved by considering this data.

The morphology of the SiO_2/Si surface has been experimentally characterized using different techniques including transmission electron microscopy (TEM) and atomic force microscopy (AFM).[8–11] It has been suggested that only correlation lengths below $\sim$1.5 nm could explain the observed dependence of electron and hole mobility on strain at high electric fields.[7,10] It was also suggested that AFM measurements would not be able to detect such short wavelength undulations due to the finite AFM tip diameter as the tip diameter cuts off the high frequency components of the surface roughness.[10] High resolution nanoscale analysis is therefore necessary to filter out the long wavelength surface undulations and concentrate on the high frequency components (short wavelength undulations).

In this work, we have studied the impact of uniaxial and biaxial strains on the surface roughness of silicon wires and strained silicon-on-insulator (sSOI) films by AFM using a super sharp tip (typical radius $\sim$2 nm). The AFM images have been filtered to suppress the long wavelength undulations of the surface roughness. The self-affinity of uniaxial and biaxial strained silicon surfaces has been analyzed using a multiple scan-based technique.[21–23] This allows the self-affine behavior of a surface to be determined by considering multiple areas of different sizes on the same sample. The RMS roughness, correlation length, and Hurst exponent parameters have been extracted and the dependency of these parameters on strain and surface roughness wavelength has been identified. Strain levels ranging from 0% to 2.3%, the range of strain utilized in present CMOS technology, have been investigated. The induced strain is varied and controlled by using structures with different geometries fabricated on the same chip. This technique has been used to successfully characterize the fracture strength, Young's modulus, and piezoresistance of silicon beams with thicknesses varying from 200 nm down to 50 nm under tensile stress.[24–26] The results provide evidence that surface roughness parameters vary with strain and these parameters are dependent on the type (uniaxial, biaxial) and level of strain.

The paper is organized as follows. Section II describes the theory and background of self-affine surfaces and the roughness parameters. Section III presents the fabrication details of the wires and SOI films and describes the AFM multiple scan technique. Section IV presents the main results of the AFM surface roughness measurements in the strained wires and SOI films. A thorough analysis concerning the validity of the power spectral density (PSD) and autocorrelation function models used to describe the surface roughness is presented. This is followed by a discussion surrounding the dependency of roughness parameters on strain and wavelength of the surface roughness. The main conclusions are summarized in Sec. V.

II. THEORY

The SiO_2/Si interface can be well described as a self-affine surface.[16,27] A surface is self-affine, if the surface looks the same (or statistically the same) after performing an anisotropic dilation and rescaling of the different dimensions.[19,28] This type of scaling is characteristic of fractal objects.[17] The height profile of a self-affine surface is described by the singled-value function[19]

$$h(x) \simeq \epsilon^{-\alpha} h(\epsilon x)\,, \tag{1}$$

where h is the height value of the surface at a position x along the x-axis, ε is the scaling factor along the x direction, and α is the Hurst exponent $(0 \leq \alpha \leq 1)$. For a real self-affine surface, however, the scaling behavior will only hold within a certain range of lengths, i.e., the height values cannot keep increasing or decreasing indefinitely. The Hurst exponent and the fractal dimension D of a fractal surface are related by[16]

$$D = 3 - \alpha\,. \tag{2}$$

The fractal dimension D is a non-integer, which measures the capacity of a fractal object to fill the space in which it is embedded.[21] In order to completely characterize the morphology of a self-affine surface, three independent parameters are necessary:[19] the interface width or standard deviation of the surface heights, the correlation length, and the Hurst exponent. The interface width Δ is defined as

$$\Delta = \sqrt{\overline{[h(\boldsymbol{r}) - \bar{h}]^2}}\,, \tag{3}$$

where $h(\boldsymbol{r})$ is the surface height at position $\boldsymbol{r}$ and $\bar{h}$ is the average height over all $\boldsymbol{r}$. It is common practice for a digitized

[This article is copyrighted as indicated in the article. Reuse of AIP content is subject to the terms at: http://scitation.aip.org/termsconditions. Downloaded to] IP: 143.106.108.185 On: Mon, 25 May 2015 13:35:19

image to shift all the sampled heights in order to have a zero-mean height. For a zero-mean height, the standard deviation of the height profile (and hence the interface width) is the same as the RMS of the height profile values. In this work, all the surface profiles are redefined to be zero-mean height and the term "RMS roughness" will be used to describe the surface height profile.

The correlation length Λ is usually determined from the autocorrelation function $R(l)$

$$R(l) = \frac{1}{\Delta^2} h(\boldsymbol{r}) h(\boldsymbol{r}+l). \tag{4}$$

Here, l is the lag distance at which the autocorrelation function is estimated. The correlation length is defined as the distance l at which $R(l)$ decays to $1/e$ of its initial value $R(0)$. The correlation length is a parameter, which estimates the onset of the lateral distance at which the surface height values are still correlated. Surface height values separated by lateral distances above the correlation length have little correlation.

Another correlation function commonly used to characterize random surfaces is the height-height correlation function, defined as

$$H(l) = (h(\boldsymbol{r}+l) - h(\boldsymbol{r}))^2. \tag{5}$$

The height-height correlation function is related to the autocorrelation functions as

$$H(l) = 2\Delta^2 [1 - R(l)]. \tag{6}$$

Several analytical functions have been proposed to model the experimental data obtained from real rough surfaces using Eqs. (4) and (5), including the Gaussian and exponential forms.[8,11] These functions, however, do not account for self-affine behavior. For a real self-affine and isotropic surface, i.e., a surface statistically invariant under a rotation transformation, an equivalent analytical expression for the height-height correlation function was proposed by Sinha *et al.*[20]

$$H(l) = 2\Delta^2 \left[1 - e^{-\left(\frac{l}{\Lambda}\right)^{2\alpha}}\right] \sim \begin{cases} 2\Delta^2, \ l \gg \Lambda, & saturation\,region \\ \propto l^{2\alpha}, \ l \ll \Lambda, & self-affine\,region. \end{cases} \tag{7}$$

Here, the Gaussian and exponential functions are represented by the particular cases of $\alpha = 1$ and $\alpha = 0.5$, respectively. Alternatively, the Hurst exponent α can be understood as the jaggedness of the surface,[18–20] which is a measure of the high frequency and low-amplitude components of the surface profile.[21] Values closer to 1 relate to smooth surfaces, whereas values closer to 0 relate to more jagged surfaces. There is no exact physical definition relating the Hurst exponent with the jaggedness or smoothness of a surface, or with the frequency components of a surface profile. Figure 1 shows two height profiles with the same RMS and correlation length values and different Hurst exponent values. The height profile of Figure 1(b) is more jagged than the profile

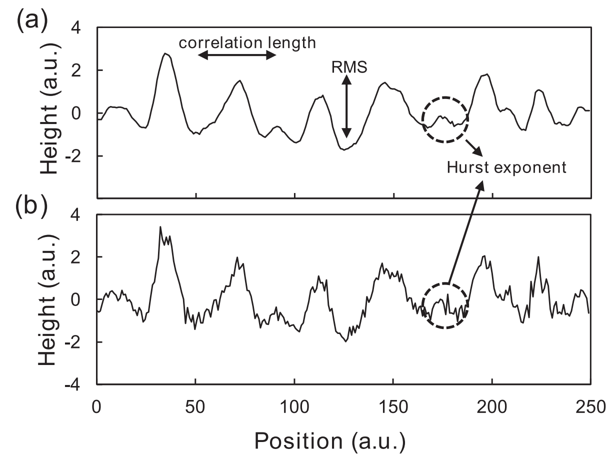

FIG. 1. Height profile of two rough surfaces (a) and (b). Both height profiles have the same RMS roughness and correlation length although different Hurst exponents. Profile (b) is more jagged than profile (a). This indicates that the Hurst exponent of profile (b) is smaller than that of profile (a).

in Figure 1(a) and therefore has a smaller Hurst exponent. Equation (7) also reflects that a real surface will only exhibit self-affine behavior within a short range $l \ll \Lambda$ and will saturate at a constant value for $l \gg \Lambda$. From the relation between the height-height correlation functions (Eqs. (6) and (7)), the functional form of the autocorrelation function proposed by Sinha *et al.*[20] for a self-affine surface is

$$R(l) = e^{-\left(\frac{l}{\Lambda}\right)^{2\alpha}}. \tag{8}$$

The height-height correlation function has been traditionally used to extract the roughness parameters from a digitized surface image such as an AFM image.[8,29,30] However, due to the scale dependence of Eqs. (4) and (5) with a self-affine surface, extracting the roughness parameters from a single scan may result in erroneous values.[21,23] An alternative procedure based on multiple scans was proposed by Vicsek *et al.*[22] In this approach, the roughness parameters are extracted from measurements of the interface width from areas with different lateral lengths. For a real self-affine surface, the scale dependence of the interface width can be fitted using the expression[21,23]

$$\Delta(L) = \Delta_0 \sqrt{1 - e^{-\left(\frac{L}{\Lambda}\right)^{2\alpha}}} \sim \begin{cases} \Delta_0, \ L \gg \Lambda, & saturation\,region \\ \propto L^{\alpha}, \ L \ll \Lambda, & self-affine\,region. \end{cases} \tag{9}$$

Here, L is the lateral scan length and Δ_0 is the true interface width of the scanned surface. For a self-affine surface and lateral scan lengths large enough, a semi-log plot of $\Delta(L)$ against lateral length L will show two distinct regions (Figure 2). The self-affine region at low values of L is scale dependent with L^{α}. The saturation region at high values of L is scale independent with a constant value $\Delta(L) = \Delta_0$. In some cases, the self-affine region will also exhibit a bending region at small values of the scan length due to the shortage of data at small scan areas. Due to the asymptotic behavior, there is no precise boundary between the saturation and the

[This article is copyrighted as indicated in the article. Reuse of AIP content is subject to the terms at: http://scitation.aip.org/termsconditions. Downloaded to] IP: 143.106.108.185 On: Mon, 25 May 2015 13:35:19

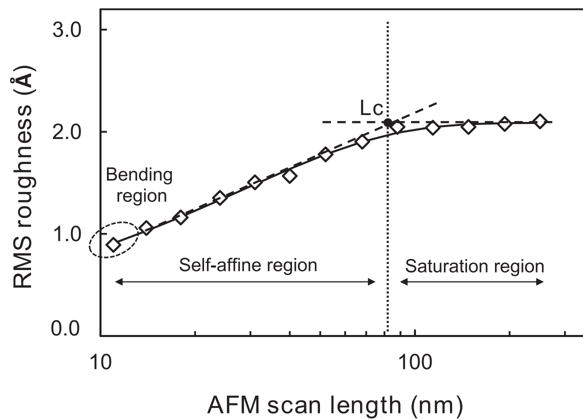

FIG. 2. Self-affine and saturation region. L_c is defined as the intersection between the asymptotic lines of the saturation and self-affine regions. At small scan lengths, there is a slight bending due to the shortage of data of the scanned area.

self-affine region. In this work, the intersection L_c between the asymptotic lines of the saturation and self-affine regions has been used to define the boundary between the saturation and the self-affine regions (Figure 2). The asymptotic line for the saturation region (plateau) has been modeled with a horizontal line crossing the RMS roughness value at the maximum scan length ($L = 250$ nm). The self-affine region has been modeled with a straight line tangent at the inflexion point between the end of the self-affine region and the beginning of the bending zone. The variations of L_c will be used to estimate the impact of strain on the surface morphology in the horizontal direction and the results will be compared with the variations in correlation length.

III. METHODOLOGY

Five uniaxially strained silicon samples and two biaxially strained silicon samples were investigated. The uniaxially strained samples consisted of five silicon free-standing beams 2 μm- wide aligned along the [110] direction and fabricated on an SOI wafer. Details of the SOI fabrication process can be found elsewhere.[35] An oxide layer was thermally grown above the silicon film and thereafter used as a mask for patterning the silicon into beams. The tensile stress was induced by a silicon nitride beam attached to the end of the silicon sample. The silicon nitride was deposited by low pressure chemical vapor deposition at 800 °C. Upon cooling after deposition, the silicon nitride experiences thermal stress. HF 73% was used to etch the buried oxide and release the beams. After the release process, the silicon nitride undergoes an internal stress relaxation. This induces a tensile stress in the silicon beams due to the difference in thermal expansion coefficients between silicon nitride ($\alpha_{Si3N4} \sim 5 \times 10^{-6}$ K^{-1}) and silicon ($\alpha_{Si} \sim 2 \times 10^{-6}$ K^{-1}).[31,32]

Five levels of strain were investigated: 0.2%, 0.6%, 1.3%, 2.0%, and 2.3%. The strain levels were verified by scanning electron microscopy (SEM) and Raman spectroscopy and compared with analytical calculations and finite element simulations.[33,34] The silicon crystal structure of the samples was also analyzed and concluded that it has not been compromised.[34] Strain determined by SEM was carried out by measuring the displacement of a mobile cursor fabricated alongside the silicon beams with respect to a fixed cursor positioned at the substrate sidewalls. Additional details of the fabrication process and strain characterization can be found in Refs. 31 and 34, respectively. The uniaxially tensile strained silicon samples *will be referred to hereafter* as the "uniaxial samples."

The biaxially strained silicon on insulator (sSOI) samples consisted of a 14 nm-thick biaxial tensile strained silicon layer on top of a 145 nm buried oxide layer. Two strain levels were investigated: 0.8% and 1.3%. Unstrained SOI samples having equal oxide and silicon thickness as the sSOI samples were also analyzed. Both the unstrained and the biaxially strained SOI samples *will be referred to hereafter* as the "biaxial samples." Details of the SOI and sSOI fabrication process can be found elsewhere.[35] The strain levels were verified by Raman spectroscopy. Before the analysis, the SOI and sSOI samples were cleaned with a 2:1 solution of H_2SO_4:H_2O_2 for 10 min and HF 1% for 15 s. The short cleaning time and the low HF concentration are known to have a minimum impact on the silicon surface, while still removing the native oxide and organic residues.[36]

Surface roughness was characterized by AFM using an XE-150 model from Park Systems. A super-sharp silicon tip with a radius ~2 nm was used. Three areas of 250×250 nm^2 separated by ~10 μm were analyzed for each sample. Only zero and first order regression polynomial fitting were required for the image flattening process. The image resolution was 512×512 pixels. This setup results in a scan step of ~0.5 nm/pixel.

All the AFM measurements were performed in non-contact mode within an acoustic isolation enclosure and on anti-vibration table to minimize the noise background. The non-contact mode was preferred over the contact mode due to the fragile nature of the samples (free-standing beams withstanding large values of strain (up to 2.3%)). The noise floor (baseline noise) was measured before and at the end of the measurements. In a noise floor measurement, the scan size is set at 0×0 nm^2, while the tip-sample working distance and the scan-rate are set at the same values as those for a topography measurement. The response signal for this one-point scan measurement is the noise floor of the instrument. The RMS of the noise floor was ~0.2–0.3 Å.

The dependence of the RMS roughness on scan length was characterized by progressively scaling each scanned area (250×250 nm^2) to a minimum scan length of ~10 nm. This resulted in 12 square areas with scan lengths scaled with a factor ~1.3 (Figure 3(a)). To increase accuracy and account for roughness variations with the sample orientation, the scan areas were scaled from five different directions. One scaling was performed from the center towards the corners of the image (Figure 3(a)). The other remaining four scaling were performed from each corner of the image towards the diagonally opposite corner (Figure 3(b)). Thus, $3 \times 5 \times 12 = 180$ areas for each sample were analyzed. The RMS value of the height profile for each scan length was determined from the average of all equal size areas, i.e., $3 \times 5 = 15$ areas.

[This article is copyrighted as indicated in the article. Reuse of AIP content is subject to the terms at: http://scitation.aip.org/termsconditions. Downloaded to] IP: 143.106.108.185 On: Mon, 25 May 2015 13:35:19

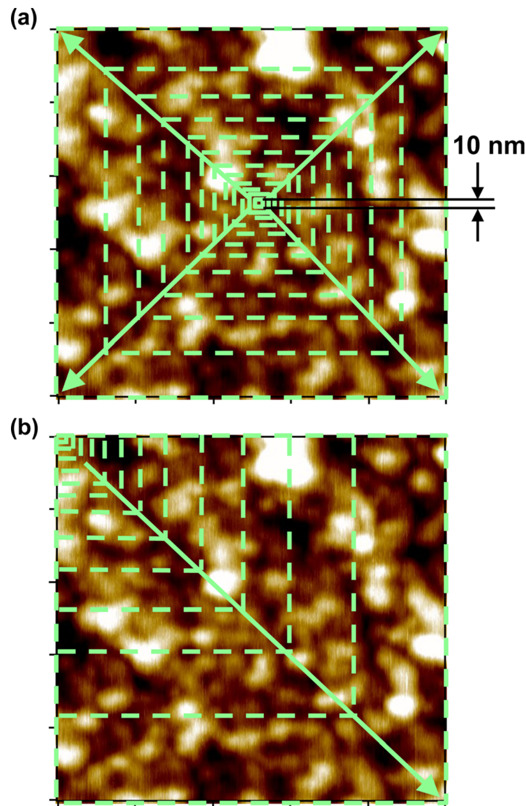

FIG. 3. Scaling of the AFM images from different directions (minimum lateral dimension ~10 nm). (a) Scaling direction relative to the center of the image. (b) Scaling direction relative to the top-left corner.

IV. RESULTS AND DISCUSSION

In order to analyze the impact of strain on the high frequency components of the surface roughness profile (necessary to explain electron and hole mobility at high electric fields), the AFM images were filtered using a high-pass filter. A high-pass filter suppresses the surface undulations having wavelengths larger than the cut-off wavelength. For the uniaxial samples, the AFM images were filtered using cut-off wavelengths of 50, 30, and 20 nm. For the biaxial samples, only the 50 nm cut-off wavelength was investigated. Below 20 nm for the uniaxial samples and 50 nm for the biaxial samples, the signal-to-noise ratio was less than 3 dB. Wavelengths above 50 nm were not considered since the effect of the filter on the surface profile was negligible.

The unfiltered images were also analyzed and compared with the filtered images. Figure 4 shows the effect of a high-pass filter with a cut-off wavelength of 50 nm on the surface roughness of a 0.2% uniaxially strained sample. The long wavelength undulations observed in the original surface profile (smooth line in Figure 4(a)) are suppressed in the filtered profile (Figure 4(b)). However, the rectangular areas in Figure 4(b) show that the high frequency components (short wavelength undulations) are still discernible after the filtration. This confirms that the initial high frequency components of the surface profile are present in the filtered profile and only the low frequency components are suppressed.

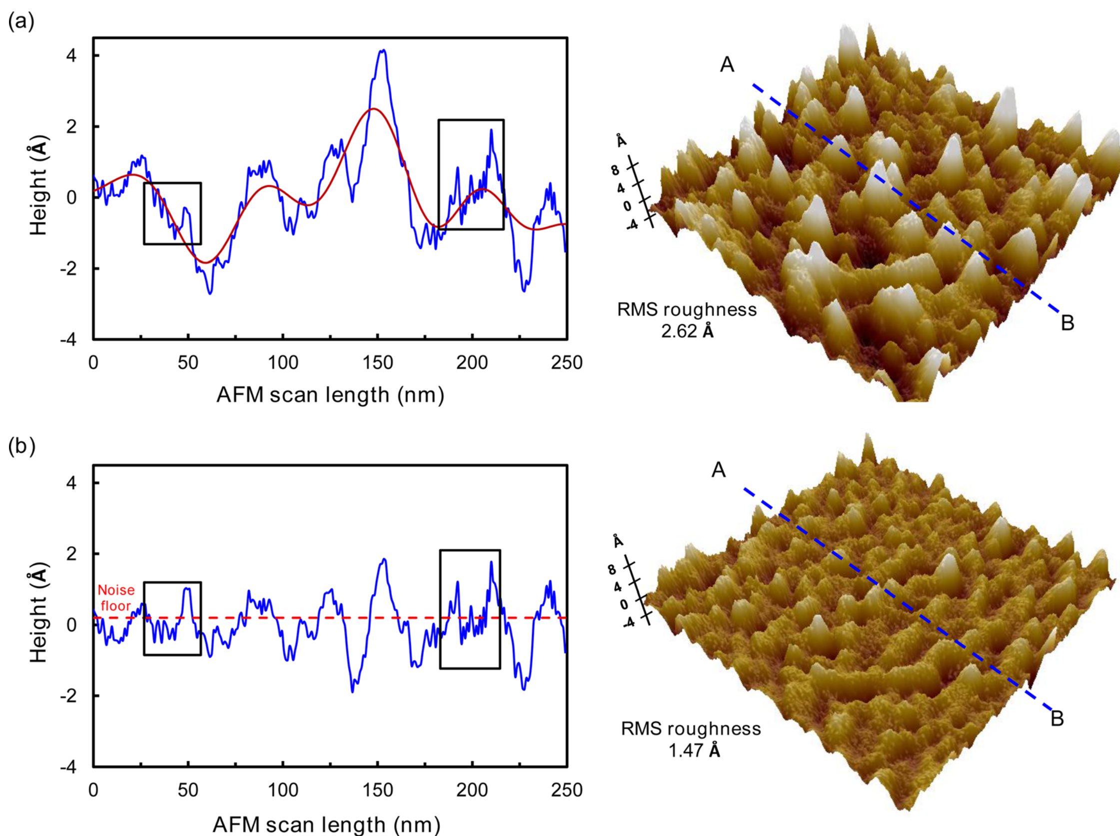

FIG. 4. Effect of a high-pass filter with a cut-off wavelength of 50 nm on the surface roughness of a 0.2% uniaxially strained sample. Height profile across segment A-B and 3D view (a) before filtering and (b) after applying the filter. The filter eliminates the wavelength undulations above the cut-off wavelength (smooth solid line in height profile (a)). After the filtration, the small features present in the original profile and the low wavelength undulations are still discernible (rectangular areas).

[This article is copyrighted as indicated in the article. Reuse of AIP content is subject to the terms at: http://scitation.aip.org/termsconditions. Downloaded to] IP: 143.106.108.185 On: Mon, 25 May 2015 13:35:19

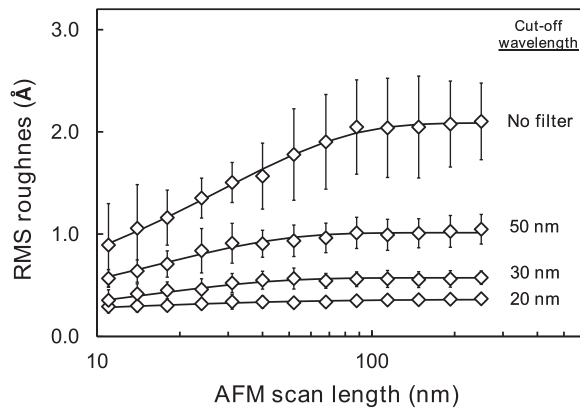

FIG. 5. Variation in RMS roughness of a 2.0% uniaxially strained sample with the scan length for the unfiltered and filtered surface roughness profiles.

A. Roughness in sSOI wires (uniaxial samples)

Figure 5 shows the variation in RMS roughness of the wires with the scan length and with the filter cut-off wavelength. There is a decrease in RMS roughness with decreasing filter cut-off wavelength. This is because the number of frequency components suppressed by a high-pass filter increases with decreasing filter cut-off wavelength. The error bars in Figure 5 represent the deviation from the mean (standard deviation) of the experimental data. At areas smaller than $\sim 100 \times 100\,\text{nm}^2$, the RMS roughness exhibits scale dependency with the scan length. This confirms that the strained silicon surface is self-affine and scan length dependency must be considered when determining the surface roughness parameters, including the RMS roughness, correlation length, and Hurst exponent.

The roughness parameters were determined by fitting the experimental data with a weighted least-square (chi-squared) non-linear regression and the model described by Eq. (9) (solid lines in Figure 5). Matlab 7.10 (R2010a) was used for the fitting procedure. Figure 6 shows the variation in RMS roughness with the scan length for the 50 nm cut-off wavelength filtered images and strain values in the range 0.2%–2.3%. All the graphs exhibit the characteristic asymptotic behavior described by Eq. (9) for a real self-affine surface: there is a saturation region characterized by a plateau where the RMS values are constant, and a self-affine region where the RMS values scale with the lateral scan length. In all cases (filtered and unfiltered images), an increase of L_c (the intersection between the saturation and the self-affine regions) with increasing strain is observed (Figure 6). This suggests that the surface roughness undulations are expanding horizontally with strain. Figure 6 also shows that the RMS roughness decreases with increasing strain. The reduction in RMS roughness with increasing strain is most likely related to the increase of L_c with strain, i.e., a horizontal expansion of the surface roughness undulations coincides with a reduction in the RMS roughness amplitude.

Figure 7 shows the variation in RMS roughness (Δ_0 in Eq. (9)) with uniaxial strain after fitting the experimental data for all the wavelength regimes. There is a progressive decrease in RMS roughness as the strain is increased from 0% to 2.3% at all the wavelength regimes. The reduction in RMS roughness varies between 20% and 40% corresponding to the non-filtered and 30 nm cut-off wavelength filtered images, respectively. The biaxial data shown in Figure 7 will be discussed in Sec. IV B.

The variation in correlation length (Λ in Eq. (9)) with strain determined after fitting the experimental data is shown in Figure 8. There is a significant increase in correlation length as strain increases from 0% to 2.3% at all wavelength regimes. This agrees with the hypothesis that surface undulations expand horizontally, while shrinking in the vertical direction. The increase in correlation length varies between 130% and 150% (corresponding to the 20 nm and 50 nm cut-off wavelength filtered images, respectively). The increase in correlation length appears more pronounced for high values of strain ($\varepsilon > 2.0\%$). For example, the increase in correlation length for the non-filtered images is $\sim$8 nm/% strain in the range 0.2%–2.0% strain, compared with an increase of $\sim$63 nm/% strain in the range 2.0%–2.3% strain. This agrees with previous observations[9] where large variations in correlation length were found to be initiated at strain values higher than $\sim$1.7%. This suggests that a threshold value of strain may exist after which the impact of the strain on the topography becomes more significant. The correlation length decreases with decreasing filter cut-off wavelength because a

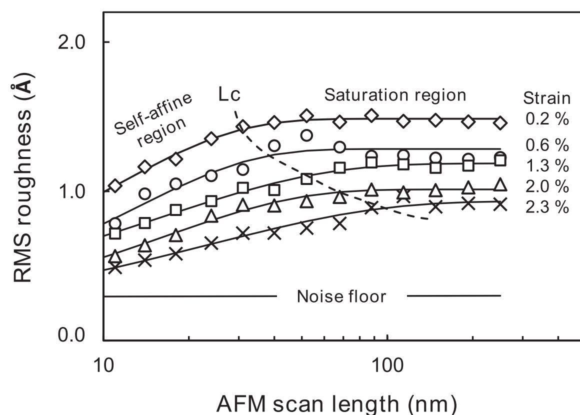

FIG. 6. Variation in RMS roughness of the 50 nm cut-off wavelength filtered images with the scan length and strain values in the range 0.2%–2.3%. An increase of L_c with increasing strain (dashed line) is observed.

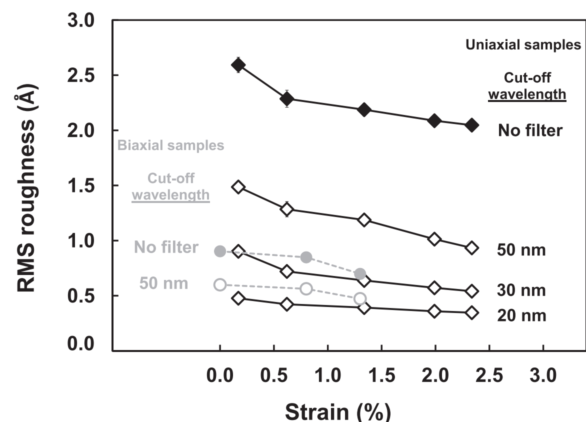

FIG. 7. Variation in RMS roughness with strain for the uniaxial and biaxial samples at different filter cut-off wavelengths. The RMS roughness decreases with strain at all wavelength regimes (filter cut-off wavelength).

[This article is copyrighted as indicated in the article. Reuse of AIP content is subject to the terms at: http://scitation.aip.org/termsconditions. Downloaded to] IP: 143.106.108.185 On: Mon, 25 May 2015 13:35:19

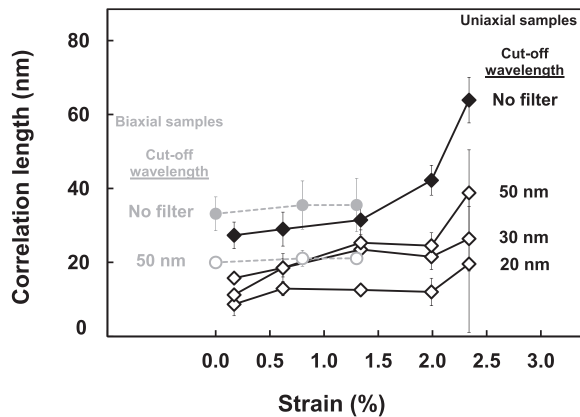

FIG. 8. Variation in correlation length with strain for the uniaxial and biaxial samples at different filter cut-off wavelengths. The correlation length of the uniaxial samples increases with strain at all wavelength regimes (filter cut-off wavelength). The increase is more pronounced at high values of strain. The correlation length of the biaxial samples is relatively constant.

high-pass filter suppresses the undulations with wavelengths above the cut-off wavelength. The biaxial data shown in Figure 8 will be discussed in Sec. IV B.

The variation in Hurst exponent (α in Eq. (9)) with strain and with filter cut-off wavelength (determined from the fitting procedure) is shown in Figure 9. For the non-filtered and the 50 nm cut-off wavelength filtered images, the Hurst exponent is relatively constant between ~0.5–0.6 in the range of strain 0.2%–2.3% (Figures 9(a) and 9(b)). This indicates that the surface roughness can be reasonably well represented by the exponential model ($\alpha = 0.5$) in Eq. (9). For a cut-off wavelength of 30 nm and 0.2% strain (Figure 9(c)), the Hurst exponent is ~0.8. In this case, the surface roughness is better described by the Gaussian model ($\alpha = 1$) in Eq. (9). However, at 2.3% strain, the Hurst exponent reduces to ~0.4 (close to the exponential model). For a cut-off wavelength of 20 nm (Figure 9(d)), the Hurst exponent is also found to decrease for increasing strain. The Hurst exponent decreases from ~0.6 at 0.2% strain to ~0.2 at 2.3% strain. At this cut-off wavelength (20 nm) and strain (2.3%), neither the exponential nor the Gaussian models can successfully describe the surface roughness. These low values of Hurst exponent may be explained by considering that the high frequency components of the background noise will have a more significant impact on the Hurst exponent for data filtered with a 20 nm cut-off wavelength than for unfiltered data or for data filtered with a higher cut-off wavelength (i.e., 30 or 50 nm).

The large variations in Hurst exponent (ranging from $\alpha = 0.8$ to $\alpha = 0.2$, shown in Figure 9) indicate that the Hurst exponent might be dependent on the strain and the surface undulations wavelength. However, the variations may also be related to the variations in correlation length and RMS roughness with strain (Figures 7 and 8). Figure 10 shows it is possible that the impact of strain on the high frequency undulations (jaggedness) of the surface profile may be smaller (or even negligible) compared with the impact of strain on the low frequency undulations of the surface profile. Therefore, an increase of the correlation length would be mainly

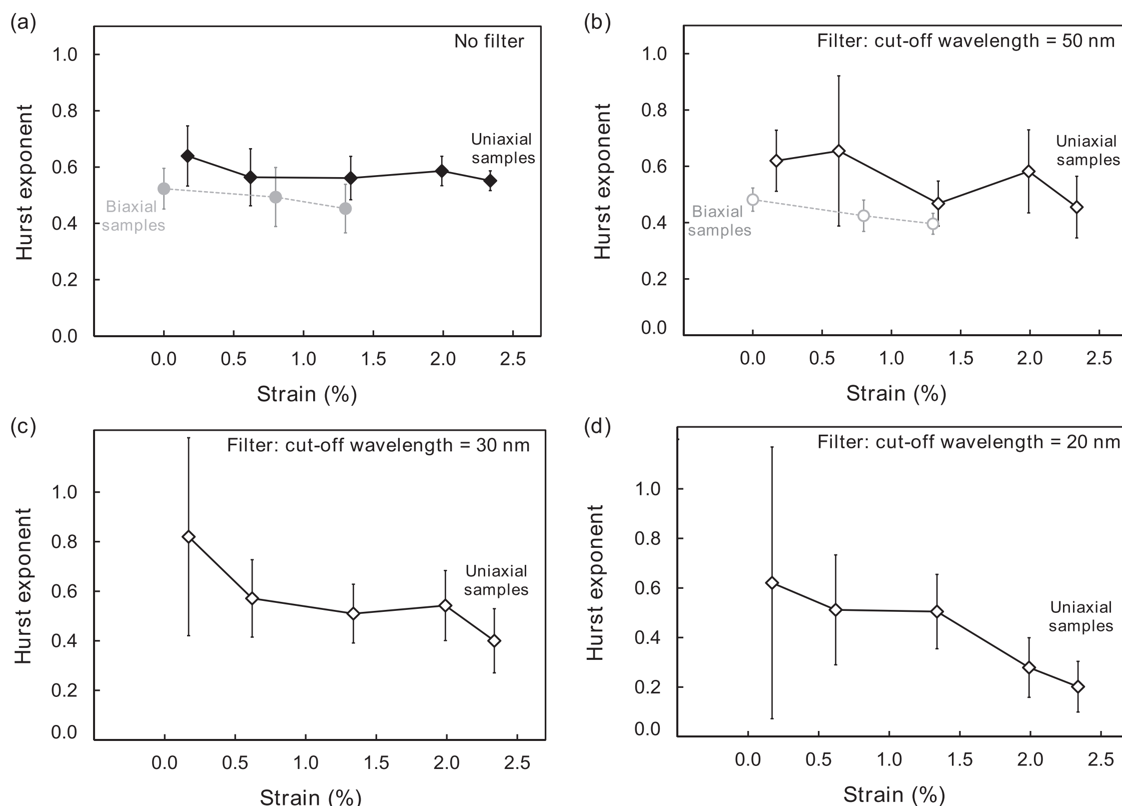

FIG. 9. Variation in Hurst exponent with strain for the (a) unfiltered, (b) 50 nm, (c) 30 nm, and (d) 20 nm cut-off wavelength filtered images. For the unfiltered (a) and 50 nm cut-off wavelength filtered images (b), the Hurst exponent of the uniaxial and biaxial samples is relatively constant (~0.6–0.4). For the 30 nm (c) and 20 nm (d) cut-off wavelength filtered images, the Hurst exponent of the uniaxial samples significantly varies (~0.8–0.2).

[This article is copyrighted as indicated in the article. Reuse of AIP content is subject to the terms at: http://scitation.aip.org/termsconditions. Downloaded to] IP: 143.106.108.185 On: Mon, 25 May 2015 13:35:19

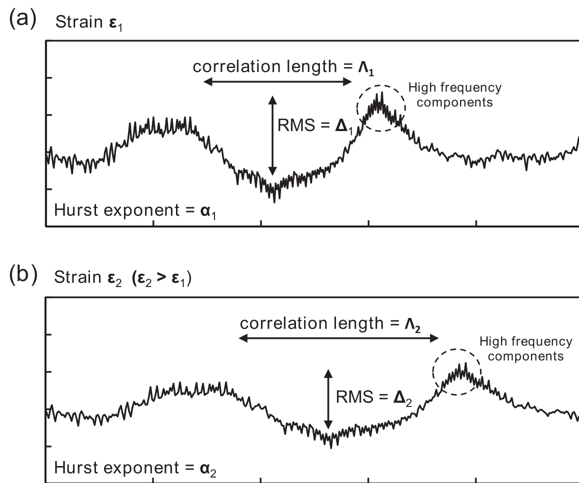

FIG. 10. Schematic showing the impact of tensile strain on the RMS roughness, correlation length, and Hurst exponent. The applied tensile strain and the correlation length are smaller in (a) than in (b). The RMS roughness in (a) is higher than in (b). Assuming that the impact of strain is higher on the long-wavelength undulations of the surface roughness profile compared to that on the short-wavelength undulations (jaggedness), the low frequency components of the surface roughness profile in (b) will increase compared to those in (a). The high frequency components, however, will have a smaller impact. The difference between the high and low frequency components in (b) will increase as compared to those in (a) and as a result, the Hurst exponent in (b) will be smaller than in (a).

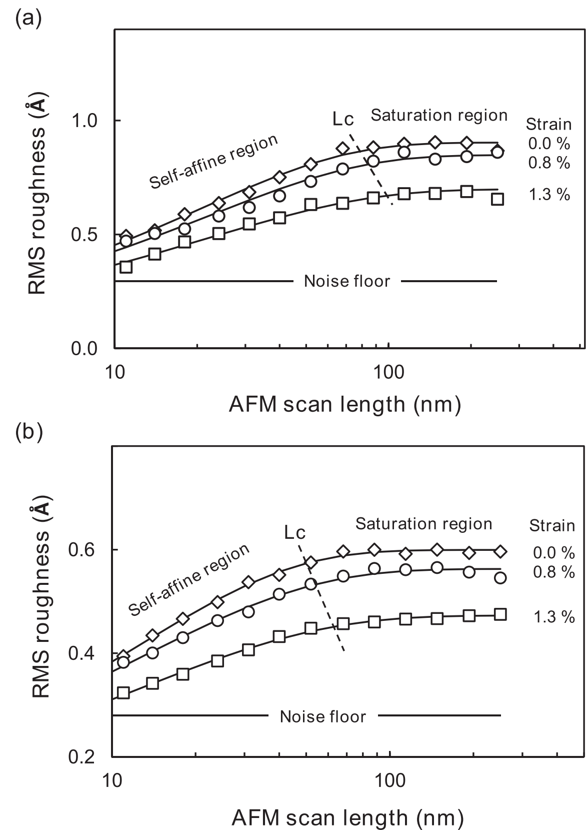

FIG. 11. Variation in RMS roughness of the SOI (strain 0%) and sSOI (strain 0.8% and 1.3%) samples with scan length for (a) unfiltered and (b) 50 nm cut-off wavelength filtered images. A similar increase (∼30%) of L_c (dashed line) with increasing strain is observed for the unfiltered and filtered images. This increase is smaller to that of the uniaxial samples (∼50%) with a 50 nm cut-off wavelength filtration within similar range of strain (0.2%–1.3%).

ascribable to an increase of the long wavelengths undulations (low frequency components) with little contribution from the short wavelengths undulations (high frequency components). The jaggedness of the surface at high values of strain (Figure 10(a)) would then appear enhanced (Hurst exponent would decrease) compared with the jaggedness of the surface at low values of strain (Figure 10(b)).

The uncertainties in Hurst exponent (error bars in Figure 9) are large, especially at low values of strain. This may indicate that the AFM technique is approaching the limits and/or the model used (Eq. (9)) may not be sufficient to determine the Hurst exponent accurately. Figure 9 nevertheless demonstrates that different strain levels and analysis (wavelength regime) will yield differing Hurst exponents, with data switching between Gaussian and exponential models. This work therefore explains (and justifies) why some models use Gaussian and some use exponential to fit the experimental data in carrier mobility models. This is discussed further in Sec. IV C.

B. Roughness in SOI and sSOI films (biaxial samples)

Figure 11 shows the variation in RMS roughness with scan length in the SOI and sSOI biaxial samples with no filter (Figure 11(a)) and after applying a 50 nm cut-off wavelength filter (Figure 11(b)). Both SOI and sSOI films show the self-affine and saturation regions. For the unfiltered images (Figure 11(a)), the intersection between the self-affine and the saturation regions, L_c, varies from ∼75 nm to 95 nm (∼30% increase) as strain is increased from 0% to 1.3%. A similar increase in L_c with strain is found for the filtered images (Figure 11(b)). The ∼30% increase in L_c is similar to that obtained for the unfiltered uniaxial samples (∼25%, data not shown) for a similar range of strain (0.2%–1.3%). However, for the 50 nm cut-off wavelength filtered uniaxial samples (Figure 6), the increase in L_c is ∼50% (∼100% for the 30 nm cut-off wavelength filtered uniaxial samples). This suggests that at the 50 nm wavelength regime, the undulations on the biaxial sSOI films expand less than uniaxial samples for the same range of strain. Nevertheless, the different fabrication process undergone by the samples and the different types of strain (uniaxial and biaxial) may also have an impact on the differences in L_c.

Figure 7 shows the variation of RMS roughness with biaxial strain for the non-filtered and the 50 nm cut-off wavelength filtered images. There is a small reduction in RMS roughness with increasing biaxial strain. The RMS roughness reduces from ∼0.9 Å to 0.7 Å for the non-filtered images and from ∼0.6 Å to 0.5 Å for the filtered images as strain is increased from 0% to 1.3%. The RMS roughness of the biaxial samples is overall lower than for the uniaxial samples and may be explained by the different fabrication processes of the samples. The uniaxial samples have undergone etching in HF and thermal oxidation, which are known to increase the RMS roughness of initial silicon smooth surface.[36] Only mild cleaning was performed on the biaxial samples, which is unlikely to affect the silicon surface (Sec. III). In percentage (Figure 12), however, no significant changes in RMS

[This article is copyrighted as indicated in the article. Reuse of AIP content is subject to the terms at: http://scitation.aip.org/termsconditions. Downloaded to] IP: 143.106.108.185 On: Mon, 25 May 2015 13:35:19

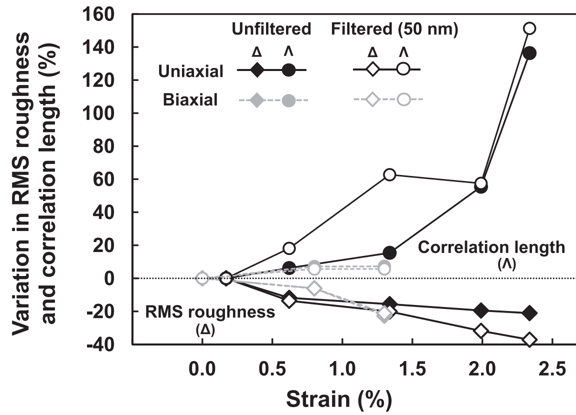

FIG. 12. Percentage variation in RMS roughness and correlation length with strain for the uniaxial and biaxial samples compared with 0% strain. There is no significant variation in RMS roughness between the uniaxial and biaxial samples in the range 0%–1.3% strain. The correlation length, however, varies significantly between the uniaxial and biaxial samples filtered with a 50 nm cut-off wavelength in the range 0%–1.3% strain. It is possible that changes in the topography in the biaxial samples occur at strain values above 1.3%.

roughness between the uniaxial and biaxial samples with strain are observed over a similar range of strain (0%–1.3%). There is a 25% (21%) reduction in RMS roughness for the unfiltered (50 nm filtered) biaxial samples and a 16% (20%) reduction for the unfiltered (50 nm filtered) uniaxial samples.

The variation in correlation length with biaxial strain is shown in Figure 8. For the filtered and non-filtered images, the correlation length is constant in the range 0%–1.3%. In contrast, as shown in Figure 12, the uniaxial samples exhibit an increase in correlation length of 15% (unfiltered images) and ~63% (50 nm cut-off wavelength filter) for the range of strain 0%–1.3%. These values are also in agreement with the variations in L_c determined above and indicate that biaxial strain may have a smaller impact on the correlation length than uniaxial strain. However, it is still possible that major changes in the topography occur at values of strain higher than 1.3% (as observed with the uniaxial samples at values of strain higher than ~2.0%, Figures 8 and 12). Samples with high biaxial strain (>1.3%) were not available in this study.

Conventional fabrication processes in commercial SOI and sSOI wafers may involve some finishing steps, e.g., chemical mechanical polishing (CMP), which may mask or modify changes in the surface roughness, including the correlation length, due to the strain.[35,37] Tensile strain is induced in the uniaxial strained silicon beams after the final release process and the surface does not undergo further polishing. Therefore, strain-induced changes in roughness parameters may be more prominent in the uniaxial samples. Nevertheless, differences in the finishing steps during the fabrication process of the SOI and sSOI wafers, e.g., application of a touch polishing, may be also behind the differences in the surface roughness of the uniaxial and biaxial samples.

The Hurst exponent of the biaxial samples was also investigated and found to be relatively constant at ~0.4–0.5 for the filtered and non-filtered images in the range 0%–1.3% of strain (Figure 9). This value of Hurst exponent indicates that the roughness surface distribution of the biaxial samples is well represented by the exponential model. Furthermore, these values are the same as the uniaxial samples for the same wavelength regime.

C. Surface roughness models

The surface roughness-limited mobility μ_{SR} is usually determined from the inverse relation with the PSD[8,10]

$$\mu_{SR} \propto \frac{1}{S(q)} . \tag{10}$$

Here, S is the PSD and q is the wave vector in reciprocal space. Figure 13 shows the PSD for the uniaxial samples with 0.2% and 2.3% strain and for the biaxial samples with 0% and 1.3% strain (the PSD for the uniaxial samples with 0.8%, 1.3%, and 2.0% and for the biaxial samples with 0.8% of strain lie between the limiting curves depicted in Figure 13). For the uniaxial samples, the contribution of the low frequency components ($q <\sim 2 \times 10^{-2}$ nm^{-1}) in the PSD is more pronounced for the samples with high values of strain, i.e., for a given frequency, the PSD increases with increasing strain. In contrast, for a given frequency in the range $\sim 2 \times 10^{-2} \leq q \leq \sim 1 \times 10^{-1}$ nm^{-1}, the PSD slightly decreases with increasing strain. At frequencies $q >\sim 1 \times 10^{-1}$ nm^{-1}, the PSD for all samples converges (due to the finite size of the AFM tip). These results agree with the hypothesis (Sec. IV A) that the large variations in Hurst exponent with increasing strain for the uniaxial samples observed in Figure 9 may be related with an increase of the long wavelengths undulations (low frequency components) with increasing strain but with little contribution from the short wavelengths undulations (high frequency components). For the biaxial samples, however, the PSD at a given frequency (Figure 13), does not exhibit significant changes with strain varying in the range 0%–1.3%. This also confirms the results in Sec. IV B for the

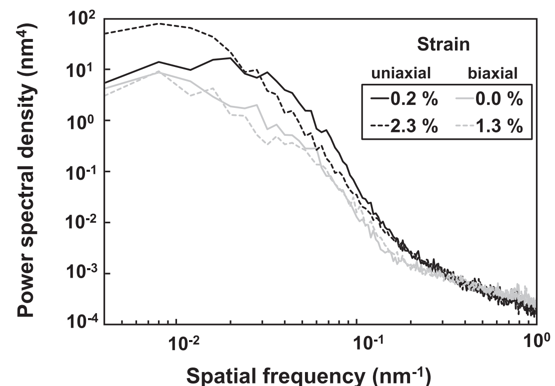

FIG. 13. Power spectral density for the uniaxial and biaxial samples. Only the minimum and maximum values of strain are presented, i.e., 0.2% and 2.3% for the uniaxial samples and 0.0% and 1.3% for the biaxial samples. The PSDs of the uniaxial samples with 0.8%, 1.3%, and 2.0% strain lie between the 0.2% and 2.3% curves. For the uniaxial samples, the PSD at a given frequency $q <\sim 2 \times 10^{-2}$ nm^{-1} increases with increasing strain. At frequencies in the range $\sim 2 \times 10^{-2} \leq q \leq \sim 1 \times 10^{-1}$ nm^{-1}, the PSD of the uniaxial samples slightly decreases with increasing strain. For the biaxial samples, however, the PSD at a given frequency does not significantly differ with strain in the range 0%–1.3%.

[This article is copyrighted as indicated in the article. Reuse of AIP content is subject to the terms at: http://scitation.aip.org/termsconditions. Downloaded to] IP: 143.106.108.185 On: Mon, 25 May 2015 13:35:19

correlation length and for the Hurst exponent, which were found to be constant with strain in the range 0%–1.3%.

Traditionally, data from mobility experiments have been fitted with the Gaussian and exponential models of the autocorrelation function or the PSD (Fourier transform of the autocorrelation function), using the RMS roughness and correlation length values as fitting parameters.[8,11,12] However, neither of these models can successfully fit the experimental mobility data determined for both holes and electrons with the same RMS roughness and correlation length values.[13] Therefore, in order to successfully fit the experimental data from electron and hole mobility using the same correlation length and RMS roughness values, alternative expressions have been suggested.[14,15] For the autocorrelation function, Isihara *et al.*[14] proposed the functional form

$$R(l) = \Delta^2 e^{-\left(\frac{l}{\Lambda}\right)^n}, \tag{11}$$

where l, Δ, and Λ, are the lag distance, interface width, and correlation length parameters. Here, n is an exponential parameter used to determine the functional form of $R(l)$. For $n = 1$, Eq. (11) reduces to the exponential form and for $n = 2$, Eq. (11) reduces to the Gaussian form. Comparing Eqs. (8) and (11), the exponential parameter n and the Hurst exponent α can be related by $n = 2\alpha$. This relation suggests that the exponential parameter n used within the autocorrelation function and PSD models[14,15] is highly connected to the jaggedness of the surface and consequently with the high frequency components of the surface profile. This therefore explains the findings in Ref. 10, where in order to describe the dependency of electrons and holes mobility at high electric fields with the surface roughness, it was concluded that higher frequency components ($q \approx 10^7$ cm^{-1}) in the surface roughness spectra were required compared with those obtained by AFM.

For a self-affine surface, the PSD has been modeled as[19]

$$S(q) = \frac{4\pi\alpha\Delta^2\Lambda^2}{\left(1 + q^2\Lambda^2\right)^{1+\alpha}}. \tag{12}$$

From Eq. (12) and from the inverse relation between μ_{SR} and the PSD (Eq. (10)), μ_{SR} is proportional to Δ^{-2}. However, μ_{SR} depends also on the correlation length Λ and Hurst exponent α. Therefore, whereas for $\alpha = 0.5$, $\mu_{SR} \propto \Lambda$, for $\alpha = 1$, $\mu_{SR} \propto \Lambda^2$. Also, the relation between the surface roughness scattering mobility μ_{SR} and the correlation length Λ depends strongly on the electron density at the inversion layer. This relation is further complicated when screening effects of electrons in the inversion layer are considered, e.g., dielectric screening.[8] Consequently, there is a large uncertainty as for the appropriate values for the surface roughness parameters required to fit the electron and hole mobility in electronic devices. The surface roughness parameters may also depend on factors such as the type of strain (uniaxial and biaxial), sign (compressive and tensile), and crystal orientation of the substrate.[2,7,38] As an example, values for the correlation length in the range 3–30 Å in biaxially strained inversion layers are commonly reported.[7,8,10,39] However, as discussed in Ref. 7 only values for the correlation length $\Lambda < \sim 15$ Å, would fit the "universal mobility" curve and consequently explain the observed dependence of electron and hole mobility on strain at high electric fields.

Finally, most models used to describe the PSD from experimental data, including Eq. (12), assume that the roughness parameters entering the model are uncorrelated. This may not be always the case and the roughness parameters might have some degree of correlation induced by factors such as the fabrication process, AFM artifacts, and strain. Thus, in order to determine the surface roughness mobility, it is important to understand the different factors affecting the roughness parameters, which enter the PSD. This will be discussed in Sec. IV D.

D. Factors affecting the surface roughness parameters

Roughness parameters are highly dependent on the statistical functions used to fit the experimental data (Eq. (9)), order of the flattening process used to correct for AFM artifacts and sample tilt and length of the available data.[8,11] Stommer *et al.*[21] analyzed the changes in morphology due to wet chemical etching of the (100) silicon surface using the multiple scan technique and Eq. (9) to fit the experimental data. Large variations in the correlation length (from 18 nm to 145 nm) and in the Hurst exponent (from 0.40 to 0.95) were found depending on whether a single or multiple scan technique was used. It was concluded[21] that the flattening process used to correct the tilt of the sample favored the accumulation of the height data in the self-affine region. This could lead to wrong results when using the single scan technique to determine the roughness parameters. They also concluded that due to a finite scan-size, wavelength undulations longer than the scan length are cut off, and consequently the correlation length is underestimated. In contrast, more reliable results were obtained using the multiple scan technique and Eq. (9) to fit the experimental data. This is because Eq. (9) accounts for the self-affine behavior and is less sensitive to limited data since it only relies on RMS roughness measurements to determine the roughness parameters.

From the AFM measurements performed in this work, the RMS roughness, correlation length, and Hurst exponent are shown to vary with strain and the wavelength regime (Secs. IV A and IV B). The variation in roughness parameters with the wavelength regime indicates that the data are also highly dependent on the fabrication process and treatments undergone by the sample.[21] The dependency of the roughness parameters identified, and especially the changes in Hurst exponent, with the wavelength regime (also found in Ref. 21) may explain the inconsistencies of the exponential parameter n found in Ref. 14 for different silicon interfaces.

The results show that numerous factors including the strain, wavelength regime, fabrication process, technique used for measuring the parameters and image processing all affect the roughness parameters.

V. CONCLUSIONS

This work has investigated the impact of strain on the SiO_2/Si interface roughness at the nanoscale under uniaxial

[This article is copyrighted as indicated in the article. Reuse of AIP content is subject to the terms at: http://scitation.aip.org/termsconditions. Downloaded to] IP: 143.106.108.185 On: Mon, 25 May 2015 13:35:19

and biaxial strains. Samples with 0%–2.3% strain, which encompasses the range of strain used in the channel regions of state-of-the-art CMOS technology, have been analyzed by AFM. The results show that the SiO_2/Si interface is self-affine (surface roughness shows scaling fractal behavior) and significantly changes with the applied strain.

The analysis of roughness at the nanoscale has been possible by filtering the AFM images with a high-pass filter and using three cut-off wavelengths (50, 30, and 20 nm) and a multiple scan technique. The RMS roughness decreases with increasing uniaxial and biaxial strains, and the reduction is dependent on the strain level. For the uniaxial samples, a reduction of ~40% in RMS roughness was observed as the strain was increased from 0.2% to 2.3%, (filtered with a 30 nm cut-off wavelength filter, which was the minimum detectable wavelength). However, over similar same range of strain (from 0% to 1.3%), the uniaxial and biaxial samples (unfiltered and filtered with a 50 nm cut-off wavelength filter) experienced the same reduction in RMS roughness (~15%–25%).

An analysis of the self-affinity has further allowed us to determine the variation in correlation length and Hurst exponent (used to describe a self-affine surface) due to uniaxial and biaxial strains. These parameters are likely to impact mobility and have to be considered in carrier transport models. The correlation length was found to increase with increasing uniaxial strain. This was more pronounced for higher values of strain. The increase in correlation length per percentage of strain in the range 2.0%–2.3% strain was ~63 nm/%, compared with ~8 nm/% in the range 0.2%–2.0% strain. The percentage change in correlation length with strain was equivalent for filtered and unfiltered images. This suggests that a threshold value of strain may exist at ~2.0% after which the sensitivity of correlation length to strain increases. For the biaxial samples, the variation in correlation length in the range 0%–1.3% strain was negligible.

The Hurst exponent was also shown to change with strain, and was affected differently by uniaxial and biaxial samples. For a 30 nm filter cut-off wavelength, the Hurst exponent of samples with low levels of uniaxial strain (0.2%) is ~0.8 (close to the Gaussian model $\alpha = 1$), whereas for high levels of strain (2.3%), the Hurst exponent is ~0.4 (close to the exponential model $\alpha = 0.5$). This suggests the models used to represent the strained silicon surface should be modified according to the level of strain. For the biaxial samples, the Hurst exponent was found to be constant at ~0.5 for all the strain values and wavelength regimes (exponential model $\alpha = 0.5$). The error in Hurst exponent determined by AFM and/or the model used however, indicated that the technique might be limited to accurately determine the Hurst exponent variations at the nanoscale.

The Hurst exponent has also been shown to relate to the exponent parameter n used in some models of the PSD and autocorrelation functions for the surface roughness scattering limited-mobility. The dependence of the Hurst exponent on the wavelength regime and the relationship identified with the exponent parameter n may explain the different n values found on different silicon interfaces.[14] The work indicates that carrier transport models for strained silicon MOSFETs operating at high electric fields such as present CMOS technology should include the RMS roughness, correlation length, and Hurst exponent as fitting parameters in order to account for the self-affine behavior of the SiO_2/Si interface.

ACKNOWLEDGMENTS

The authors would like to acknowledge the financial support from the Engineering and Physical Sciences Research Council (EPSRC).

[1] Y. Song, H. Zhou, Q. Xu, J. Luo, H. Yin, J. Yan, and H. Zhong, J. Electron. Mater. **40**, 1584 (2011).
[2] M. L. Lee, E. A. Fitzgerald, M. T. Bulsara, M. T. Currie, and A. Lochtefeld, J. Appl. Phys. **97**, 011101 (2005).
[3] M. Chu, Y. K. Sun, U. Aghoram, and S. E. Thompson, Annu. Rev. Mater. Res. **39**, 203 (2009).
[4] Y. Zhao, M. Takenaka, and S. Takagi, IEEE Electron Device Lett. **30**, 987 (2009).
[5] Z. Y. Cheng, M. T. Currie, C. W. Leitz, G. Taraschi, E. A. Fitzgerald, J. L. Hoyt, and D. A. Antoniadas, IEEE Electron Device Lett. **22**, 321 (2001).
[6] K. Rim, J. L. Hoyt, and J. F. Gibbons, IEEE Trans. Electron Devices **47**, 1406 (2000).
[7] M. V. Fischetti, F. Gamiz, and W. Hansch, J. Appl. Phys. **92**, 7320 (2002).
[8] O. Bonno, S. Barraud, D. Mariolle, and F. Andrieu, J. Appl. Phys. **103**, 063715 (2008).
[9] E. Escobedo-Cousin, S. H. Olsen, T. Pardoen, U. Bhaskar, and J.-P. Raskin, Appl. Phys. Lett. **99**, 241906 (2011).
[10] A. Pirovano, A. L. Lacaita, G. Ghidini, and G. Tallarida, IEEE Electron Device Lett. **21**, 34 (2000).
[11] S. M. Goodnick, D. K. Ferry, C. W. Wilmsen, Z. Liliental, D. Fathy, and O. L. Krivanek, Phys. Rev. B **32**, 8171 (1985).
[12] G. Mazzoni, A. L. Lacaita, L. M. Perron, and A. Pirovano, IEEE Trans. Electron Devices **46**, 1423 (1999).
[13] Y. Zhao, H. Matsumoto, T. Sato, S. Koyama, M. Takenaka, and S. Takagi, IEEE Trans. Electron Devices **57**, 2057 (2010).
[14] T. Ishihara, K. Matsuzawa, M. Takayanagi, and S. I. Takagi, Jpn. J. Appl. Phys., Part 1 **41**, 2353 (2002).
[15] A. Pirovano, A. L. Lacaita, G. Zandler, and R. Oberhuber, Int. Electron Devices Meet. Tech. Dig. **1999**, 527.
[16] T. Yoshinobu, A. Iwamoto, K. Sudoh, and H. Iwasaki, J. Vac. Sci. Technol. B **13**, 1630 (1995).
[17] B. B. Mandelbrot, *The Fractal Geometry of Nature: Updated and Augment* (W. H. Freeman and Company, 1982).
[18] M. Pelliccione and T.-M. Lu, *Evolution of Thin-film Morphology: Modeling and Simulations* (Springer, Dordrecht, 2007).
[19] Y. P. Zhao, G. C. Wang, T.-M. Lu, M. D. Graef, and T. Lucatorto, *Characterization of Amorphous and Crystalline Rough Surface: Principles and Applications* (Elsevier Science, 2000).
[20] S. K. Sinha, E. B. Sirota, S. Garoff, and H. B. Stanley, Phys. Rev. B **38**, 2297 (1988).
[21] R. Stommer, A. R. Martin, T. Geue, H. Goebel, W. Hub, and U. Pietsch, Adv. X-Ray Anal. **41**, 101 (1999).
[22] T. Vicsek, M. Cserző, and V. K. Horváth, Physica A **167**, 315 (1990).
[23] J. C. Arnault, A. Knoll, E. Smigiel, and A. Cornet, Appl. Surf. Sci. **171**, 189 (2001).
[24] U. K. Bhaskar, V. Passi, S. Houri, E. Escobedo-Cousin, S. H. Olsen, T. Pardoen, and J.-P. Raskin, J. Mater. Res. **27**, 571 (2012).
[25] V. Passi, U. K. Bhaskar, T. Pardoen, U. Sodervall, B. Nilsson, G. Petersson, M. Hagberg, and J. P. Raskin, J. Microelectromech. Syst. **21**, 822 (2012).
[26] U. K. Bhaskar, T. Pardoen, V. Passi, and J.-P. Raskin, Appl. Phys. Lett. **102**, 031911 (2013).
[27] X. H. Liu, J. Chen, M. Chen, and X. Wang, Appl. Surf. Sci. **187**, 187 (2002).
[28] T. Vicsek, *Fractal Growth Phenomena*, 2nd ed. (World Scientific, 1992).
[29] J. B. Da Silva, Jr., E. A. De Vasconcelos, B. E. C. A. Dos Santos, J. A. K. Freire, V. N. Freire, G. A. Farias, and E. F. Da Silva, Jr., Microelectron. J. **36**, 1011 (2005).
[30] Z. J. Liu, N. Jiang, Y. G. Shen, and Y. W. Mai, J. Appl. Phys. **92**, 3559 (2002).

[This article is copyrighted as indicated in the article. Reuse of AIP content is subject to the terms at: http://scitation.aip.org/termsconditions. Downloaded to] IP: 143.106.108.185 On: Mon, 25 May 2015 13:35:19

[31]S. Gravier, M. Coulombier, A. Safi, N. Andre, A. Boe, J.-P. Raskin, and T. Pardoen, J. Microelectromech. Syst. **18**, 555 (2009).
[32]R. F. Bunshah, *Handbook of Deposition Technologies for Films and Coatings—Science, Technology and Applications*, 2nd ed. (William Andrew Publishing/Noyes, 1994).
[33]F. Ureña, S. H. Olsen, L. Šiller, U. Bhaskar, T. Pardoen, and J.-P. Raskin, J. Appl. Phys. **112**, 114506 (2012).
[34]F. Ureña, S. H. Olsen, and J.-P. Raskin, J. Appl. Phys. **114**, 144507 (2013).
[35]B. Ghyselen, J. M. Hartmann, T. Ernst, C. Aulnette, B. Osternaud, Y. Bogumilowicz, A. Abbadie, P. Besson, O. Rayssac, A. Tiberj, N. Daval, I. Cayrefourq, F. Fournel, H. Moriceau, C. D. Nardo, F. Andrieu, V. Paillard, M. Cabié, L. Vincent, E. Snoeck, F. Cristiano, A. Rocher, A. Ponchet, A. Claverie, P. Boucaud, M. N. Semeria, D. Bensahel, N. Kernevez, and C. Mazure, Solid-State Electron. **48**, 1285 (2004).
[36]L. Lai and E. A. Irene, J. Appl. Phys. **86**, 1729 (1999).
[37]W. Schwarzenbach, N. Daval, S. Kerdilès, G. Chabanne, C. Figuet, S. Guerroudj, O. Bonnin, X. Cauchy, B. Y. Nguyen, and C. Maleville, in Proceedings of the IEEE International Conference on Integrated Circuit Design and Technology (Austin, TX, USA, 2012).
[38]Y. H. Xie, G. H. Gilmer, C. Roland, P. J. Silverman, S. K. Buratto, J. Y. Cheng, E. A. Fitzgerald, A. R. Kortan, S. Schuppler, M. A. Marcus, and P. H. Citrin, Phys. Rev. Lett. **73**, 3006 (1994).
[39]M. De Michielis, F. Conzatti, D. Esseni, and L. Selmi, IEEE Trans. Electron Devices **58**, 3219 (2011).

[This article is copyrighted as indicated in the article. Reuse of AIP content is subject to the terms at: http://scitation.aip.org/termsconditions. Downloaded to] IP: 143.106.108.185 On: Mon, 25 May 2015 13:35:19